Materials Horizons

ROYAL SOCIETY OF CHEMISTRY

COMMUNICATION

View Article Online
View Journal

Check for updates

Cite this: DOI: 10.1039/d5mh00512d

Received 21st March 2025,
Accepted 18th June 2025

DOI: 10.1039/d5mh00512d

rsc.li/materials-horizons

A layer-by-layer assembled superhydrophobic composite aerogel for rapid and high-capacity removal of microplastics from beverages†

Qiyue Zhao,[a] Xingxu Jiang,[b] Ergen Bao,[c] Hong-Man Hou,[a] Gong-Liang Zhang[a] and Jingran Bi *[ab]

The hierarchical integration of porous materials with rigid frameworks and biopolymer components enhances their adsorption performance. While combining porous substances with cellulose nanofibers (CNFs) to create high-performance hybrid aerogels holds significant potential, achieving this remains challenging due to suboptimal interfacial bonding and insufficient structural reinforcement from CNFs. In this study, a superhydrophobic composite aerogel ($AG^{U6\text{-}(OH)_2}$@PMSQ) was synthesized using a sequential bottom-up and layer-by-layer *in situ* growth strategy based on a robust dual-network structure formed by the "egg-box structure" and CNFs. The hierarchical porosity and superhydrophobicity of $AG^{U6\text{-}(OH)_2}$@PMSQ provided excellent adsorption capacity and sensitivity for polystyrene microplastics (PSM). The adsorption kinetics revealed that the adsorption capacity for PSM reached an impressive 555.556 mg g^{-1} within a short timeframe of 100 min. D–R model analysis indicated that hydrophobic interactions were the primary driving force behind the adsorption of PSM by $AG^{U6\text{-}(OH)_2}$@PMSQ. Meanwhile, simulation calculations confirmed that hydrogen bonding and C–H$\cdots\pi$ interactions also contribute to the adsorption process. Furthermore, $AG^{U6\text{-}(OH)_2}$@PMSQ demonstrated exceptional adsorption stability, reproducibility, and a high PSM removal rate in aqueous matrices. This innovative research offers a new insight for contaminant control in complex matrix environments.

New concepts

The integration of porous materials with rigid frameworks and biopolymer components enhances adsorption performance. While combining porous substances with cellulose nanofibers (CNFs) to develop high-performance hybrid aerogels holds great promise, challenges persist due to weak interfacial bonding and insufficient structural reinforcement by CNFs. In this study, we synthesized a superhydrophobic composite aerogel ($AG^{U6\text{-}(OH)_2}$@PMSQ) using a sequential bottom-up and layer-by-layer *in situ* growth strategy. This approach leveraged a robust dual-network structure formed by the "egg-box" framework and CNFs, ensuring enhanced stability and functionality. The hierarchical porosity and superhydrophobicity of $AG^{U6\text{-}(OH)_2}$@PMSQ enabled excellent adsorption capacity and sensitivity for polystyrene microplastics (PSM). Adsorption kinetics revealed that the material achieved an impressive adsorption capacity of 555.56 mg g^{-1} within just 100 min.

Introduction

In recent years, the use of plastic materials in food packaging has been steadily increasing.[1] These materials are prone to gradual degradation into microplastics (MPs) during food processing and storage, which refer to particles smaller than 5 mm.[2,3] Due to their persistent, non-biodegradable nature, MPs are rapidly entering the human environment, posing serious risks to public health. Polystyrene microplastics (PSM) are commonly found in beverage packaging.[4] Beyond their inherent hazards, PSM particles can act as carriers for heavy metals, toxic organic pollutants, and pathogens. This leads to the formation of microplastic complex pollutants (MCPs), which are even more harmful to both organisms and humans.[5,6] Thus, efficient removal of PSM from the food matrix is critical for promoting the sustainable development of human health. Although PSM can be removed from the environment through methods like free radical oxidation or microbial decomposition, incomplete degradation often leads to secondary contamination.[7,8] Therefore, finding effective, non-destructive methods for PSM removal remains a significant challenge.

---

[a] *SKL of Marine Food Processing & Safety Control, National Engineering Research Center of Seafood, Collaborative Innovation Center of Seafood Deep Processing, Liaoning Key Lab for Aquatic Processing Quality and Safety, School of Food Science and Technology, Dalian Polytechnic University, Dalian, 116034, China. E-mail: bijingran1225@foxmail.com*

[b] *School of Materials Science and Engineering, Beihang University, Beijing, 100191, China*

[c] *School of Materials Science and Engineering, Northeastern University, Shenyang, 110819, China*

† Electronic supplementary information (ESI) available. See DOI: **https://doi.org/10.1039/d5mh00512d**

Multifunctional adsorbent materials have gained attention for the removal of various organic and inorganic hazardous materials due to their low operating cost, high adsorption capacity, and environmental friendliness.[3,9] Materials such as hydrogel actuators, metal hydroxides, biochar, and sponges have been widely applied to remove PSM from various environments. Lan *et al.* successfully developed a zirconium foam material based on metal–organic frameworks, achieving a PSM removal efficiency of up to 95.5% in water.[10] Chen *et al.* prepared a natural, biodegradable sponge with high mechanical strength using plant proteins through chemical cross-linking, resulting in an 81.2% removal rate within 12 h for PSM.[1] However, current PSM removal methods often require lengthy adsorption processes and are challenging to reuse, which could lead to secondary pollution. Therefore, more efficient and eco-friendly approaches for PSM removal are still needed to address these limitations.

Cellulose nanofiber (CNF) aerogels are widely used as adsorbents for hazardous substances in liquid environments due to their light weight, high strength, large specific surface area, and high potential for functionalization.[11,12] However, those with a single network are often limited in mechanical strength, adsorption capacity, and surface chemistry diversity. To enhance their performance and expand their applicability in adsorption applications, further optimization in design and treatment is needed. Metal–organic frameworks (MOFs) are porous materials formed by the coordination of metal ions/clusters with organic ligands. Their structures offer a high specific surface area, easy functionalization, and high stability.[13] By incorporating MOFs into CNF substrates and creating composites with hierarchical porosity and macroscopic flexibility, the adsorption capacity of these materials can be significantly improved.[14,15] However, in mixed systems like aqueous solutions or sewage, hydrophobic materials preferentially adsorb hydrophobic substances while minimizing interference from hydrophilic substances, thus enhancing their efficiency.[16,17] Due to the comparatively weak intermolecular interactions between CNFs, hydrophobic aerogels can be produced through various methods, including chemical cross-linking,[18] layer-by-layer electrostatic coating,[19] and silylated grafting.[20] Among these, the use of organoalkoxysilanes, such as methyltrimethoxysilane (MTMS), to hybridize composite oxides is particularly promising for creating high-performance hydrophobic aerogels. Controlled hydrolysis and condensation of MTMS allow the hydrophilic silanol groups (Si–OH) to form strong bonds between polymethylsilsesquioxane (PMSQ) and the matrix. This process enables the hydrophobic methyl group ($Si–CH_3$) to transform the matrix's inherent hydrophilicity into hydrophobicity.

In this study, we developed a composite aerogel ($AG^{U6-(OH)_2}$@PMSQ) with hierarchical porosity and superhydrophobicity, utilizing an "egg-box structure" and a network of CNFs to form a stable dual-network aerogel. The proposed fabrication procedure exploited robust 3D entangled CNF networks and *in situ* nanoscale heterogeneous assembly with the loading of UiO-66-$(OH)_2$ and PMSQ mesoporous networks achieved using a layer-by-layer assembly technique for the rapid and high-capacity adsorption of PSM from beverages. Adsorption kinetics and isothermal analysis revealed the rapid adsorption rate and strong adsorption capacity of $AG^{U6-(OH)_2}$@PMSQ for PSM, and the adsorption mechanism was further explored using simulation calculations. Additionally, the adsorption stability, reproducibility, and sensitivity of $AG^{U6-(OH)_2}$@PMSQ were also evaluated. This work introduces a novel strategy for the efficient removal of PSM from beverages.

Experimental section

Materials and reagents

Zirconium chloride ($ZrCl_4$, 99.0%), 2,5-dihydroxyterephthalic acid (98.0%), *N*,*N*-dimethylformamide (DMF, 99.9%), 2,2,6,6-tetramethyl-1-piperidinyloxy (TEMPO, 98.0%), urea (99.0%), trimethoxymethylsilane (MTMS, 98.0%), cetyltrimethylammonium chloride (CTAC, 99.0%), acetonitrile (99.9%) and acetic acid (99.8%) were obtained from Macklin Co., Ltd (Shanghai, China). Polystyrene microbeads (PSM), polypropylene (PP), polyethylene terephthalate (PET), and high-density polyethylene (HDPE) (excitation wavelength: 488 nm, emission wavelength: 518 nm) were obtained from Baseline (Tianjin, China).

Synthesis of CNFs

CNFs were prepared using a modified TEMPO oxidation protocol. First, chopped filter paper was oxidized in 90 mL of sodium phosphate buffer (7.38 g, 50 mM) containing TEMPO (0.1 mM), $NaClO_2$ (10 mM), and NaClO (0.5 mL). The oxidized fibers were then washed three times with deionized water.[21,22] Following this, the suspension was processed using a high-pressure homogenizer (GEA Panda PLUS+ 2000, Gea Niro Soavl, Parma, Italy) and stored at 4 °C. The dry weight of the CNF gel was measured to be 0.60 wt%.

Synthesis of $AG^{U6-(OH)_2}$@PMSQ

Preparation of $CaCO_3$. $NaCO_3$ (0.12 M) solution was added dropwise to $CaCl_2$ (0.12 M) solution to form a turbid $CaCO_3$ (0.12 M) suspension. The mixture was then homogenized at 12 000 rpm for 30 min using an Ultra-Turrax T25 homogenizer (IKA, Wilmington, USA).

Preparation of the aerogel from CNFs (AG). By leveraging the solubility of $CaCO_3$, CNFs were combined with sodium alginate to construct a dual-network structured aerogel with enhanced stability, serving as a substrate for subsequent material assembly.

Deionized water was added to achieve final concentrations of 0.40 wt% for CNFs, 0.067% for $CaCO_3$, and 0.01% for sodium alginate (w/w).[23] 2 mL of the mixture were homogenized using a high-shear mixer at 10 000 rpm for 5 min, followed by centrifugation at 1000 rpm for 5 min to remove air bubbles. The mixture was loaded into molds and allowed to homogenize at 4 °C before being frozen overnight (−20 °C). After freezing, the molds were immersed in a 10% aqueous acetic acid solution (10 mL) for 4 h and then washed three times with 10 mL of deionized water. The samples were frozen again at −20 °C and subsequently lyophilized to remove moisture. For comparison, 0.40 wt% CNFs were homogenized at 10 000 rpm for 5 min, frozen overnight (−18 °C) and then freeze-dried to prepare aerogels with a single network structure.

Preparation of AG$^{\mathrm{U6\text{-}(OH)_2}}$. The AG was immersed in 10 mL of DMF containing $ZrCl_4$ (5.0 mM) and kept for 20 min. Then, 2,5-dihydroxyterephthalic acid (5.0 mM) and acetic acid (5 M) were added to the solution. The mixture was reacted at 120 °C for 48 h.[24] After synthesis, the aerogel was sonicated in 10 mL of DMF for 1 min to remove loosely bound MOFs. The samples were then immersed in 10 mL of acetone for solvent exchange, followed by rapid drying at 110 °C.

Preparation of AG$^{\mathrm{U6\text{-}(OH)_2}}$@PMSQ. A solution of MTMS was prepared by mixing MTMS, H_2O, acetic acid, urea, and cetyltrimethylammonium chloride (CTAC) in a mass ratio of 1 : 15 : 0.0045 : 5.0 : 0.80. The mixture was stirred for 30 min until a clear, transparent solution was obtained. Next, AG$^{\mathrm{U6\text{-}(OH)_2}}$ was immersed in 10 mL of the MTMS solution and reacted at 80 °C for 48 h.[25,26] The resulting composite aerogel was removed, washed with ethanol/water (v/v = 1/1) to eliminate residual chemicals, and then the solvent was exchanged three times with ethanol and hexane, respectively. Finally, the composite aerogel was rapidly dried at 110 °C for 5 min to obtain AG$^{\mathrm{U6\text{-}(OH)_2}}$@PMSQ.

Characterization

The chemical structures of the prepared aerogels were studied using FT-IR (PerkinElmer, Waltham, USA) and XPS (Scientific K-Alpha, Thermo, USA). Their morphology was also observed using SEM (SU8010, Hitachi, Tokyo, Japan) and TEM (JEM-2100, JEOL, Tokyo, Japan). Compression tests were performed at a rate of 1 mm min^{-1} for one loading–unloading cycle at different strains, and 10 mm min^{-1} for 10 cycles at 80% strain (TA, Stable Micro System Ltd, Godalming, UK). Thermogravimetric analysis (TGA, TG/DTA 8122, Rigaku, Tokyo, Japan) of the aerogels was carried out in air at a heating rate of 10 °C min^{-1} over the temperature range of 30–800 °C. XRD (7000S, Shimadzu, Kyoto, Japan) was used to study the crystal structure of the samples in the 2θ range of 5–60° at a scanning rate of 5° min^{-1}. A nitrogen adsorption analyzer (ASAP 2460, Micromeritics, Norcross, USA) and a mercury porosimeter (AutoPore IV 9500, Micromeritics Instrument Ltd., USA) were used to study the specific surface area and pore size structure of the aerogels. The adsorption mechanism of PMSQ on PSM was simulated using Materials Studio software. The adsorption capacity of PSM on AG$^{\mathrm{U6\text{-}(OH)_2}}$@PMSQ was obtained by DFT calculations.

Super-hydrophobicity characterizations

Contact angle tests were performed using an optical contact angle meter (DSA 30R, Kruss GmbH, Hamburg, Germany). The volume of water droplets was controlled at 5 μL. Water droplets stained with methylene blue were immersed into one side of the aerogel surface.

Oil/water separation capability

The aerogel samples were immersed into various types of oils and organic solvents (lubricating oil, pump oil, gasoline, soybean oil, chloroform, acetone, ethanol, and *N*-hexane) and equilibrated rapidly within a few seconds. The adsorption capacity was calculated using eqn (1).

$$A = \frac{(W - W_0)}{W_0} \tag{1}$$

Adsorption experiments

The adsorption kinetics were determined by immersing the AG, AG$^{\mathrm{U6\text{-}(OH)_2}}$, and AG$^{\mathrm{U6\text{-}(OH)_2}}$@PMSQ in 2 mL of 10 mg mL^{-1} PSM under dark conditions. The residual content of PSM was measured for each sample at various time points (1, 5, 10, 20, 30, 60, 100, 300, 500 and 800 min). The adsorption kinetics of AG$^{\mathrm{U6\text{-}(OH)_2}}$@PMSQ on PP, PET, and HDPE followed the same steps as described above. The adsorption of the three aerogels was analyzed using eqn (2):

$$q_t = \frac{(C_0 - C_t)V}{m} \tag{2}$$

where C_0 (mg mL^{-1}) is the original concentration, C_t (mg mL^{-1}) is the concentration after adsorption time t (min), V is the volume of the adsorption system (mL), and m is the mass of the aerogel (g).

The adsorption kinetics data were fitted using pseudo-first-order (eqn (3)), pseudo-second-order (eqn (4)) and intra-particle diffusion models (eqn (5)).

$$q_t = q_e \times (1 - e^{-k_1 t}) \tag{3}$$

$$\frac{t}{q_t} = \frac{1}{k_2 {q_e}^2} + \frac{t}{q_e} \tag{4}$$

$$q_t = k_i t^{0.5} + C_i \tag{5}$$

where q_e is the equilibrium adsorption constant of the aerogel (mg g^{-1}), q_t is the adsorption content of the target by the aerogel at different times (mg g^{-1}), C_i is the intercept of the linear curve, and k_1, k_2, and k_i are the rate constants for pseudo-first-order, pseudo-second-order, and Weber's kinetic model of intraparticle diffusion, respectively.

The adsorption capacity of the aerogel for PSM was evaluated at different initial concentrations (1, 2, 4, 6, 8, 10, 15 and 20 mg mL^{-1}) under dark conditions. Different concentrations of PSM solutions were adsorbed through the aerogel for 200 min, after which the residual PSM content in the solutions was determined using a SpectraMax M2 Multifunction microplate reader (Meigu Molecular Instrument Co., Ltd, Shanghai, China). The isothermal data were fitted using Langmuir (eqn (6)), Freundlich (eqn (7)) and Dubinin–Radushkevich (D–R) (eqn (8)) models.

$$\frac{C_e}{q_e} = \frac{1}{q_{\max} k_L} + \frac{C_e}{q_{\max}} \tag{6}$$

$$\ln q_e = \ln k_F + \frac{1}{n}\ln C_e \tag{7}$$

$$\ln q_e = \ln Q_{MAX} - K_{DR}\varepsilon^2 \tag{8}$$

where q_e is the adsorption amount of the aerogel at equilibrium (mg g^{-1}), q_{max} is the maximum theoretical adsorption value in the Langmuir model (mg g^{-1}), C_e is the concentration of PSM in the reaction system at equilibrium (mg L^{-1}), k_L is related to the adsorption energy and the affinity of the binding site (L mg^{-1}), k_F ($mg^{1-1/n}$ $L^{1/n}$ g^{-1}) and n are Freundlich constants, Q_{MAX} (mg g^{-1}) denotes the theoretical maximum adsorption amount of the adsorbent, K_{DR} (mol^2 kJ^{-2}) is the D–R isotherm constant related to the free energy of PSM sorption, and ε is the Polanyi potential. The Polanyi potential can be calculated using eqn (9):

$$\varepsilon = RT\ln\left(1+\frac{1}{C_e}\right) \tag{9}$$

where R is the universal gas constant (8.313 J mol^{-1} K^{-1}) and T is temperature (K).

Anti-interference performance of $AG^{U6\text{-}(OH)_2}$@PMSQ

NaCl, KCl, fructose, glucose, BSA, and soy protein were added to 2 mL of PSM solution (10 mg mL^{-1}), and the concentration of each compound in the system was maintained at 10 mg mL^{-1}. $AG^{U6\text{-}(OH)_2}$@PMSQ was then immersed in each solution for 200 min under dark conditions.

$AG^{U6\text{-}(OH)_2}$@PMSQ was immersed in 2 mL of PSM solution (10 mg mL^{-1}) for 200 min under dark conditions. Subsequently, the analytes were desorbed by shaking $AG^{U6\text{-}(OH)_2}$@PMSQ in 2 mL of methanol for 30 min. The material was reused in the adsorption experiments, and this cycle was performed five times.

The removal efficiency was determined using the fluorescence intensity of the solution. The removal efficiency was determined using eqn (10):

$$Q\,(\%) = \frac{(C_0 - C_e)}{C_0} \times 100\% \tag{10}$$

where C_e and C_0 represent the fluorescence intensity of PSM in the residual solution and that in the original solution, respectively.

Analysis of real samples

200 μL of PSM (100 mg mL^{-1}) was added to 1.80 mL of bottled water, Gatorade, soda drink, Sprite, coffee, and tea, respectively. $AG^{U6\text{-}(OH)_2}$@PMSQ was then placed in each sample and allowed to adsorb for 200 min. The aerogel was washed three times with 2 mL of deionized water and subsequently immersed in methanol for 30 min to desorb the analytes. Finally, the PSM content in the solutions was measured using a SpectraMax M2 Multifunction microplate reader.

Matrix effect. A series of standard working solutions (1, 2, 4, 6, 8 and 10 mg mL^{-1}) were prepared by stepwise dilution of the PSM standard stock solution with pure solvent or six beverage matrices (bottled water, Gatorade, soda drink, Sprite, coffee, and tea). The slope values of the standard curves generated in both the sample matrices and pure solvent were compared to evaluate matrix effects.

Recovery test. The test samples were spiked with PSM standard solutions in six beverage matrices (bottled water, Gatorade, soda drink, Sprite, coffee, and tea) at three concentration levels (1, 5 and 10 mg mL^{-1}). The samples were then extracted and analyzed as described previously. Measurements were repeated three times for each concentration level, and the recovery was calculated using eqn (11):

$$\text{Recovery}\ (\%) = \frac{C_b - C_a}{C_s} \times 100\% \tag{11}$$

where C_s is the spiked concentration (μg mL^{-1}) and C_a and C_b are the measured concentrations before and after the addition of the standard solution (μg mL^{-1}).

Theoretical computations

The Vienna ab initio simulation package (VASP) was employed to optimize each structure and perform self-consistent static calculations.[27–29] In this study, the generalized gradient approximation (GGA) utilizing the Perdew–Burke–Ernzerhof (PBE) functional[30] was adopted, along with the projector augmented wave (PAW) method,[31,32] which is based on plane-wave expansion. To calculate electronic occupancy, the first-order Methfessel–Paxton method was applied with a smearing width of 0.1 eV.[33] A cutoff energy of 520 eV was chosen, with an energy convergence criterion set to 1×10^{-7} eV and a force convergence threshold of 0.01 eV $Å^{-1}$. The adsorption energy is defined as follows:

$$E_{ad} = E_{all} - (E_{surface} + E_{adsorbate}) \tag{12}$$

where E_{all} (kcal mol^{-1}) represents the total energy of the adsorbent/adsorbate system after structural optimization. $E_{surface}$ (kcal mol^{-1}) and $E_{adsorbate}$ (kcal mol^{-1}) are the energies of the adsorbent and adsorbate after structural optimization.

Statistical analysis

Statistical analysis was performed using SPSS statistical software (SPSS Inc., Chicago, IL, USA), with significance set at $p < 0.05$.

Results and discussion

Synthesis of $AG^{U6\text{-}(OH)_2}$@PMSQ

Fig. 1a illustrates the fabrication pathway and strategy for the *in situ* growth of UiO-66-$(OH)_2$ on the AG. TEMPO-oxidized CNFs, which can achieve an aspect ratio of up to 100 (Fig. S1, ESI†), contain numerous carboxyl and hydroxyl groups on their surface. These groups not only chelate metal ions for gelation but also serve as functional templates for the *in situ* synthesis of MOF crystals. A mixture of CNFs, $CaCO_3$, and sodium alginate was prepared, and the AG with a double-crosslinked network was obtained through the controlled release of Ca^{2+} from acetic acid solution after freezing. Ca^{2+} acts as an ionic cross-linking agent, transforming colloidal CNFs into a uniform fibrous

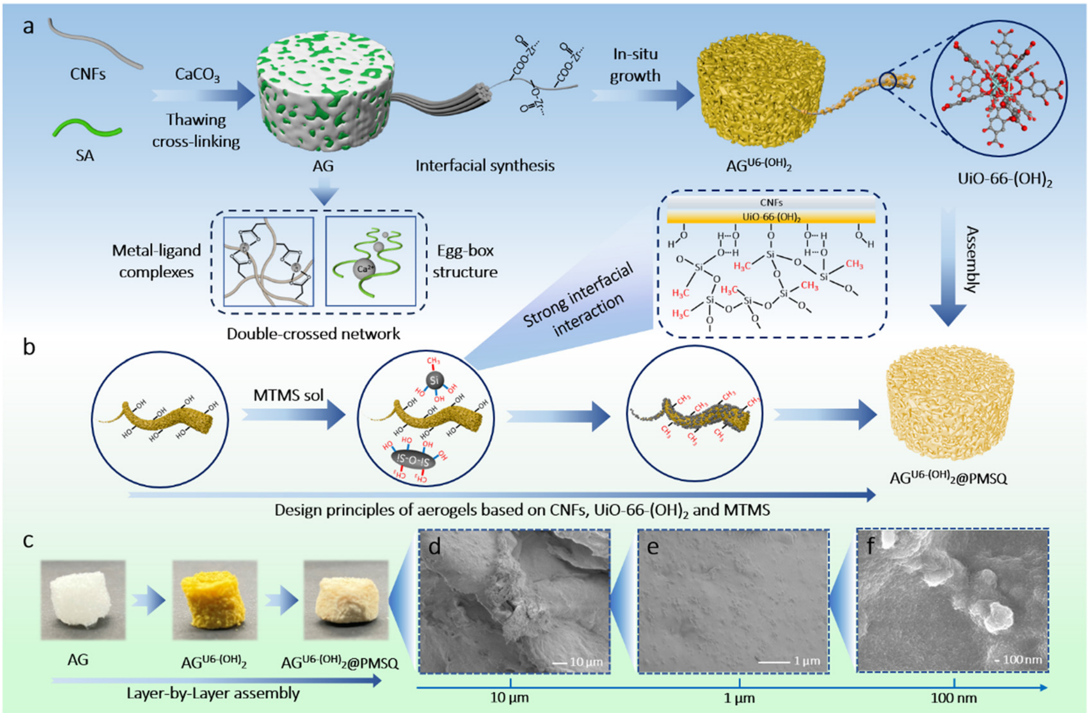

Fig. 1 (a) Schematic illustration of the fabrication process of AG$^{U6-(OH)_2}$@PMSQ involving the formation of the double-crossed network structure of the AG and the *in situ* growth of UiO-66-(OH)$_2$. (b) Schematic illustration of *in situ* polycondensation of PMSQ in the AG$^{U6-(OH)_2}$ network. (c) Images of the macrostructural evolution of aerogels during layer-by-layer assembly. (d)–(f) SEM images of AG$^{U6-(OH)_2}$@PMSQ at different scales.

network *via* electrostatic action, or it can be used with a small amount of sodium alginate to form an "egg-box structure".[23,34] These two network structures interpenetrate each other to form a fine bilayer network with excellent wet strength. The elastic strength of a single CNF network aerogel was compared to that of the AG after 12 h of water immersion (Fig. S2, ESI†). Both materials were compressed in water at 70% strain. After 10 cycles, the AG exhibited negligible strength loss and plastic deformation, whereas the single CNF network showed significant strength loss and plastic deformation.

The excellent network strength of the AG is a crucial foundation for its ability to assemble layer by layer. The AG with a defined size and shape is immersed in a solution containing Zr^{4+}, which will have ionic interactions with the carboxyl and hydroxyl groups on the CNFs.[11,35] With the addition of the ligand, AG$^{U6-(OH)_2}$ can gradually nucleate and grow on the network of CNFs. Compared to the smooth surface of the AG (Fig. S3 and S4, ESI†), UiO-66-(OH)$_2$, with its octahedral structure, is uniformly distributed across the AG$^{U6-(OH)_2}$ surface (Fig. S5, ESI†). The AG$^{U6-(OH)_2}$ particles ($\sim$200 nm) are threaded together by the CNFs, forming nanofibers with a distinctive bead-like morphology (Fig. S6, ESI†). EDS mapping shows that the Zr element is uniformly distributed on the AG$^{U6-(OH)_2}$ surface, with a content of 8.45 wt% (Fig. S7 and Table S1, ESI†).

Fig. 1b illustrates the fabrication pathway and strategy for assembling PMSQ mesoporous networks on AG$^{U6-(OH)_2}$. MTMS, a mineral precursor with one methyl and three silanol groups, was hydrolyzed and converted to colloid in the presence of an aqueous acetate catalyst. The abundant hydroxyl groups on the surface of AG$^{U6-(OH)_2}$ served as sites for *in situ* polycondensation of the precursor.[25,36] Through heat-driven polycondensation, the polymerization of the MTMS sol was promoted, resulting in the deposition of a PMSQ mesoporous network on the surfaces of AG$^{U6-(OH)_2}$. The AG$^{U6-(OH)_2}$@PMSQ product then underwent solvent exchange with a low surface tension solvent before being rapidly dried at high temperature (Fig. 1c). Fig. 1d–f shows the uniform assembly of the PMSQ mesoporous network on the AG$^{U6-(OH)_2}$ surface. The presence of UiO-66-(OH)$_2$ in the middle layer caused irregular bumps on the upper layer of PMSQ. The EDS patterns of AG$^{U6-(OH)_2}$@PMSQ reveal a uniform distribution of Zr and Si elements across the aerogel, with contents of 3.35 wt% and 22.84 wt%, respectively.

Characterization of AG$^{U6-(OH)_2}$@PMSQ

As shown in Fig. 2a, the XRD patterns of CNFs exhibit broad diffraction peaks at approximately 16° and 23°, indicating that the TEMPO-oxidized CNFs possess a typical cellulose-I crystal structure. The characteristic peaks of UiO-66-(OH)$_2$, along with *in situ* grown AG$^{U6-(OH)_2}$ and doubly-grown AG$^{U6-(OH)_2}$@PMSQ, appear at 7.4° (111), 8.5° (200), 14.8° (222), 17.1° (400), 25.8° (442), and 30.8° (711). This observation suggests that UiO-66-(OH)$_2$ successfully crystallizes and grows on the surface of CNFs, and that the subsequent growth of the PMSQ network maintains the structural integrity and properties of UiO-66-(OH)$_2$.

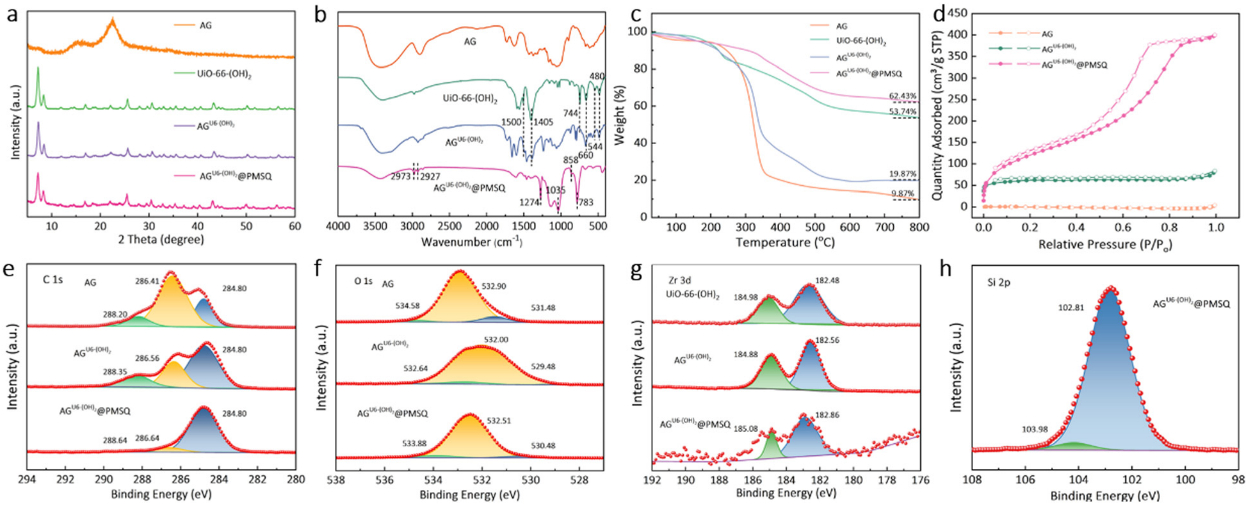

Fig. 2 Physicochemical characterization of samples, involving (a) XRD patterns, (b) FT-IR spectra, (c) TGA curves and (d) N_2 sorption isotherms. High-resolution (e) C 1s, (f) O 1s, (g) Zr 3d, and (h) Si 2p of aerogels.

As shown in Fig. 2b, the AG displays characteristic peaks of CNFs. The broad adsorption band from 3000 to 3700 cm^{-1} is attributed to the O–H stretching vibration, while the peak at 2800 cm^{-1} corresponds to the C–H stretching vibration. Two prominent peaks near 1500 and 1405 cm^{-1} represent the in-phase and out-of-phase stretching of the carboxyl groups in the UiO-66-(OH)$_2$ ligand. Additionally, peaks around 744 and 660 cm^{-1} indicate O–H and C–H stretching vibrations of the linked ligands.[37,38] The asymmetric stretching vibrations of Zr–(OC) in UiO-66-(OH)$_2$ appear at approximately 551 cm^{-1} and 485 cm^{-1}. These characteristic bands are present in both UiO-66-(OH)$_2$ and AG$^{\text{U6-(OH)}_2}$, confirming that UiO-66-(OH)$_2$ was successfully loaded into AG$^{\text{U6-(OH)}_2}$ by *in situ* growth. In AG$^{\text{U6-(OH)}_2}$@PMSQ, peaks at 2927 and 2973 cm^{-1} are associated with symmetric and asymmetric stretching vibrations of C–H bonds in the Si–CH$_3$ group. Peaks at 1274 and 858 cm^{-1} result from the asymmetric bending of the Si–C bond, indicating a methyl-rich PMSQ structure. Furthermore, absorption peaks at 783 and 1035 cm^{-1} correspond to symmetric and asymmetric stretching vibrations of Si–O–Si bonds, respectively (Fig. S9, ESI†). Notably, the intensity of the UiO-66-(OH)$_2$ characteristic peak is lower in AG$^{\text{U6-(OH)}_2}$@PMSQ than in AG$^{\text{U6-(OH)}_2}$, due to the *in situ* growth of the PMSQ network on the AG$^{\text{U6-(OH)}_2}$ surface.

TGA can be used to analyze the thermal stability of the composite aerogels. As shown in Fig. 2c, the AG exhibits significant mass loss between 220–350 °C. AG$^{\text{U6-(OH)}_2}$ exhibits mass loss at different rates in the range of 220–350 °C and 350–550 °C, which is attributed to the decomposition of CNFs and UiO-66-(OH)$_2$. Notably, AG$^{\text{U6-(OH)}_2}$@PMSQ fail to show significant mass loss at 220 °C, indicating that the CNFs in the composite aerogel still maintain a stable structure. It is not until 350 °C that the composite aerogel shows significant mass loss. The DTG curves provide a clearer view of the mass loss behavior of each sample at different temperatures. In the AG, a single CNFs decomposition event occurred between 200–350 °C. In contrast, the onset of CNFs decomposition was delayed to 250 °C in AG$^{\text{U6-(OH)}_2}$ and further to 320 °C in AG$^{\text{U6-(OH)}_2}$@PMSQ. Additionally, the decomposition peaks of CNFs in AG$^{\text{U6-(OH)}_2}$ and AG$^{\text{U6-(OH)}_2}$@PMSQ were significantly shifted to higher temperatures compared to the AG (Fig. S10, ESI†). This layer-by-layer assembly technique formed a multi-layered rigid structure on the surface of the matrix, which could greatly enhance the thermal stability of the composite aerogel.

The specific surface area and pore structure of the AG, AG$^{\text{U6-(OH)}_2}$ and AG$^{\text{U6-(OH)}_2}$@PMSQ were analyzed using N_2 adsorption–desorption analyzer. As shown in Fig. 2d, the isotherms of AG$^{\text{U6-(OH)}_2}$ and AG$^{\text{U6-(OH)}_2}$@PMSQ exhibited a sharp increase when $P/P_0 < 0.1$, indicating the presence of microporous structures that contribute to expanding the specific surface area. At $P/P_0 > 0.9$, both the AG and AG$^{\text{U6-(OH)}_2}$ showed slight N_2 adsorption, indicating the presence of macroporous structures. While AG$^{\text{U6-(OH)}_2}$@PMSQ displays a typical type IV isotherm with a marked increase in N_2 uptake at higher relative pressures, along with a clear hysteresis loop. This confirms the formation of a dense PMSQ mesoporous network on the AG$^{\text{U6-(OH)}_2}$@PMSQ surface through *in situ* assembly. The layer-by-layer assembly technique significantly increased the BET specific surface area of the aerogels, enhancing their potential performance in adsorption applications. While the AG, serving as the substrate for the composite aerogel, had a BET specific surface area of only 4.02 m^2 g^{-1}, the specific surface areas of AG$^{\text{U6-(OH)}_2}$ and AG$^{\text{U6-(OH)}_2}$@PMSQ reached 194.24 m^2 g^{-1} and 449.19 m^2 g^{-1}, respectively. Moreover, the porosity and pore size distribution (Fig. S11, ESI†) of the three aerogels were calculated using density functional theory (DFT) and Barrett–Joyner–Halenda (BJH) model. As shown in Table S2 (ESI†), the pore size distributions of the AG and AG$^{\text{U6-(OH)}_2}$ are predominantly composed of macropores (70.93%) and micropores (63.23%), while AG$^{\text{U6-(OH)}_2}$@PMSQ is primarily characterized by mesopores. The proportions of micropores, mesopores, and macropores in AG$^{\text{U6-(OH)}_2}$@PMSQ are 23.46%, 75.65% and 0.89%, respectively. This high mesoporosity is beneficial for enhancing the adsorption capacity and promoting rapid adsorption kinetics in $AG^{U6\text{-}(OH)_2}$@PMSQ.[12]

To further examine the pore structure of the aerogels, mercury intrusion porosimetry was conducted. As shown in Fig. S12 (ESI†), the mercury intrusion volumes of $AG^{U6\text{-}(OH)_2}$ and $AG^{U6\text{-}(OH)_2}$@PMSQ were significantly lower than that of the AG, likely due to the incorporation of UiO-66-$(OH)_2$ and PMSQ into the AG framework, which partially filled the pore space and reduces accessible volume. In terms of pore distribution, $AG^{U6\text{-}(OH)_2}$ and $AG^{U6\text{-}(OH)_2}$@PMSQ show a marked decrease in macropore intensity compared to the AG, while exhibiting enhanced responsiveness in the mesopore range. These findings are consistent with the N_2 adsorption–desorption analysis results.

To further investigate the assembly process of $AG^{U6\text{-}(OH)_2}$@PMSQ, the XPS spectra of various materials were compared. The XPS peaks at 532.00, 182.56, and 184.88 eV in $AG^{U6\text{-}(OH)_2}$ indicate the presence of oxygen and metal-centered zirconium in the hydroxyl group, with shifts towards low and high binding energies, respectively (Fig. 2f and g). This suggests a strong hydrogen bonding force between CNFs and UiO-66-$(OH)_2$, resulting in tight immobilization of UiO-66-$(OH)_2$ within CNFs. Meanwhile, the XPS peak area at 532.00 eV in $AG^{U6\text{-}(OH)_2}$ is significantly larger than in the AG, implying that the *in situ* grown UiO-66-$(OH)_2$ contributes numerous hydroxyl groups to the aerogel. As shown in Fig. 2e, the peak area percentage of $AG^{U6\text{-}(OH)_2}$@PMSQ at 284.80 eV is much higher than that of the AG and $AG^{U6\text{-}(OH)_2}$, which can be attributed to the enrichment of methyl groups with hydrophobic effects on the aerogel's surface after secondary assembly. The binding energy corresponding to the hydroxyl signal (532.51 eV) in the $AG^{U6\text{-}(OH)_2}$@PMSQ spectrum was higher than that in $AG^{U6\text{-}(OH)_2}$ (532.00 eV), indicating a similar strong hydrogen bonding force between the $AG^{U6\text{-}(OH)_2}$@PMSQ mesoporous network and UiO-66.[12,39] Moreover, new peaks at binding energies of 102.4 and 103.1 eV in $AG^{U6\text{-}(OH)_2}$@PMSQ can be attributed to the –Si–O– and –Si–C– groups (Fig. 2h).

Super-hydrophobic properties of $AG^{U6\text{-}(OH)_2}$@PMSQ

MTMS undergoes a polycondensation reaction on the surface of aerogels containing hydrophilic hydroxyl groups, introducing a significant number of hydrophobic groups (Fig. 3a). As a result, the superhydrophobic surface becomes entirely non-stick to water, with a contact angle of 157.1° (Fig. 3b). Water droplets stained with methylene blue immediately rolled off the $AG^{U6\text{-}(OH)_2}$@PMSQ surface at a very small tilt angle, exhibiting no hysteresis (Fig. 3e). Due to the abundance of hydrophilic hydroxyl groups, both the AG and $AG^{U6\text{-}(OH)_2}$ quickly immersed in water. In contrast, $AG^{U6\text{-}(OH)_2}$@PMSQ demonstrated remarkable hydrophobicity and floated on the water's surface (Fig. 3d). To further assess the high hydrophobicity of $AG^{U6\text{-}(OH)_2}$@PMSQ, high-density chloroform was used as a model oil.[40] The material rapidly absorbed the submerged chloroform without

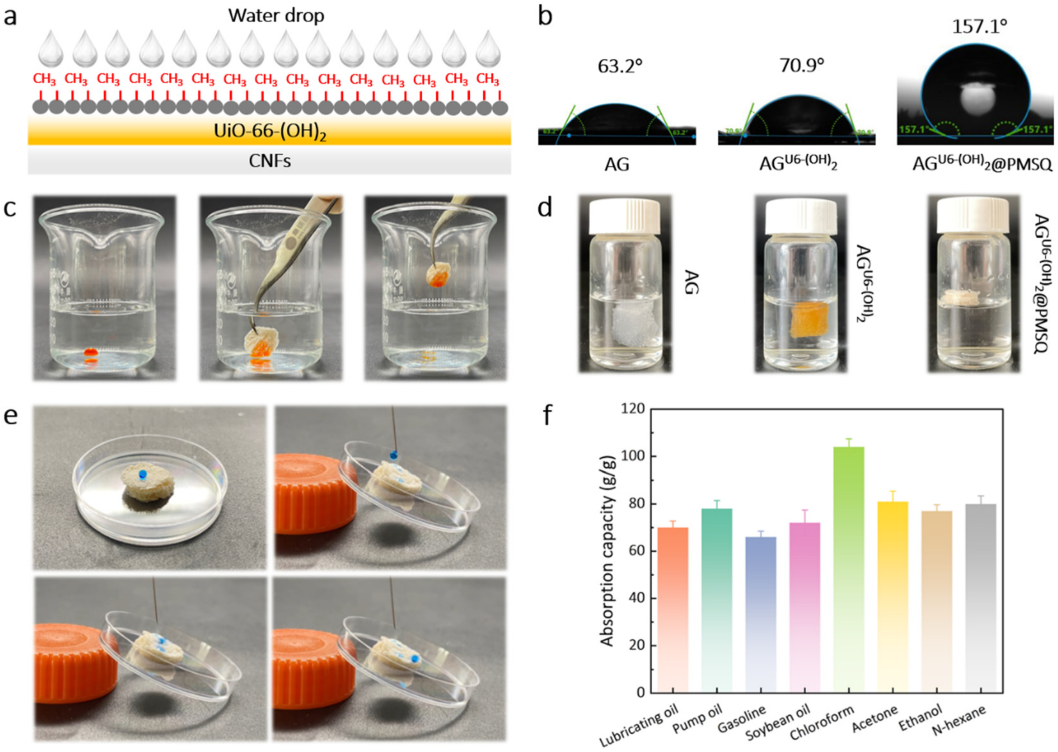

Fig. 3 Intrinsic super-hydrophobicity capability of $AG^{U6\text{-}(OH)_2}$@PMSQ. (a) Schematic diagram of $AG^{U6\text{-}(OH)_2}$@PMSQ with super-hydrophobic properties. (b) The contact angle value of the AG, $AG^{U6\text{-}(OH)_2}$, and $AG^{U6\text{-}(OH)_2}$@PMSQ. (c) Fast removal of under-water chloroform (stained with methyl red) with $AG^{U6\text{-}(OH)_2}$@PMSQ. (d) Hydrophilic and hydrophobic states of the AG, $AG^{U6\text{-}(OH)_2}$, and $AG^{U6\text{-}(OH)_2}$@PMSQ in the aqueous environment. (e) Water droplets (stained with methylene blue) rolling off from super-hydrophobic $AG^{U6\text{-}(OH)_2}$@PMSQ immediately at a small tilt angle. (f) Absorption capacity of $AG^{U6\text{-}(OH)_2}$@PMSQ by weight.

releasing it, indicating strong hydrophobicity and excellent selectivity in oil–water separation (Fig. 3c). Additionally, AG$^{\text{U6-(OH)}_2}$@PMSQ exhibits a high absorption capacity, capable of absorbing 66–104 times its own weight depending on the type of organic solvent (Fig. 3f). This absorption capacity offers a significant advantage compared to other cellulose-based nanostructured adsorbents (Table S3, ESI†).

Adsorption kinetics and adsorption isotherms

AG$^{\text{U6-(OH)}_2}$@PMSQ had a good removal effect on PSM, and the fluorescence images (Fig. 4a and b) and photographs (Fig. 4c and d) showed that PSM was hardly observed in the aqueous solution after AG$^{\text{U6-(OH)}_2}$@PMSQ adsorption. The adsorption kinetics of AG$^{\text{U6-(OH)}_2}$@PMSQ in a PSM standard solution (10 μg mL^{-1}) were evaluated, with AG and AG$^{\text{U6-(OH)}_2}$ serving as controls. As shown in Fig. 4e, the adsorption capacities of AG, AG$^{\text{U6-(OH)}_2}$ and AG$^{\text{U6-(OH)}_2}$@PMSQ increased progressively with time, reaching equilibrium after approximately 100 min. Notably, AG$^{\text{U6-(OH)}_2}$@PMSQ achieved adsorption equilibrium for PSM more quickly than with other reported adsorbents (Table S4, ESI†).

To further investigate the structural changes in AG$^{\text{U6-(OH)}_2}$@PMSQ following PSM adsorption, comparative analyses were conducted on AG$^{\text{U6-(OH)}_2}$@PMSQ before and after exposure to PSM. As shown in Fig. S13 (ESI†), SEM images reveal a substantial accumulation of PSM particles on the AG$^{\text{U6-(OH)}_2}$@PMSQ surface. EDS analysis revealed that the elements C, O, Zr, and Si were uniformly distributed throughout the aerogel. Following PSM adsorption, the relative contents of C and O increased by 6.68% and 3.26%, respectively, compared to the pre-adsorption state (Table S1, ESI†). This increase is attributed to the accumulation of PSM, which are rich in carbon and oxygen, thereby confirming the strong adsorption capacity of AG$^{\text{U6-(OH)}_2}$@PMSQ for PSM. Additionally, the FT-IR spectra of AG$^{\text{U6-(OH)}_2}$@PMSQ after adsorption retain the original characteristic peaks, indicating that the structural integrity of AG$^{\text{U6-(OH)}_2}$@PMSQ remains stable (Fig. S14, ESI†). Notably, the adsorbed AG$^{\text{U6-(OH)}_2}$@PMSQ exhibits distinct characteristic peaks at 1603 cm^{-1} and 1459 cm^{-1}, which correspond to the vibrational modes of the benzene ring skeleton. Given that the benzene ring is a key structural component of PSM, these spectral features provide further evidence of successful PSM adsorption onto AG$^{\text{U6-(OH)}_2}$@PMSQ.

To evaluate the adsorption efficiency and rate-controlling steps of the composite aerogel, the experimental data were fitted to the pseudo-first-order, pseudo-second-order, and

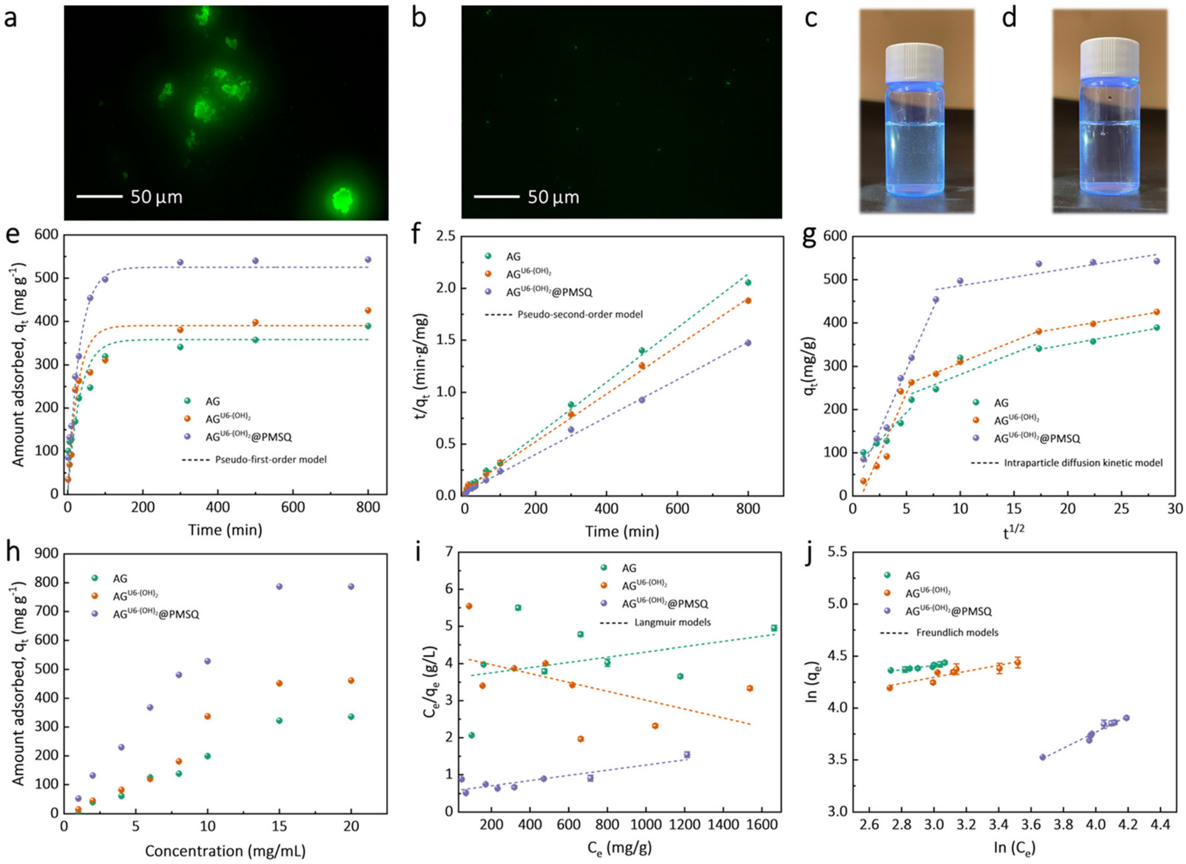

Fig. 4 Fluorescence images (a) and (b) and photographs (c) and (d) of AG$^{\text{U6-(OH)}_2}$@PMSQ before and after adsorption of PSM. Adsorption kinetics and the corresponding fitting curves based on pseudo-first-order, pseudo-second-order and intraparticle diffusion kinetic models for (e)–(g) AG, AG$^{\text{U6-(OH)}_2}$, and AG$^{\text{U6-(OH)}_2}$@PMSQ. (h) The adsorption properties of AG, AG$^{\text{U6-(OH)}_2}$, and AG$^{\text{U6-(OH)}_2}$@PMSQ on PSM at different concentrations. (i) Langmuir and (j) Freundlich isotherm modeling of the adsorption of PSM on AG, AG$^{\text{U6-(OH)}_2}$, and AG$^{\text{U6-(OH)}_2}$@PMSQ.

Weber intra-particle diffusion models, elucidating the adsorption mechanism of $AG^{U6\text{-}(OH)_2}$@PMSQ on PS. As shown in Tables S5 and S6 (ESI†), the adsorption kinetics of the three adsorbents were better described by the pseudo-second-order kinetic model, though the pseudo-first-order model also fit well, with correlation coefficients (R^2) of 0.8962 for AG, 0.9242 for $AG^{U6\text{-}(OH)_2}$, and 0.9711 for $AG^{U6\text{-}(OH)_2}$@PMSQ. This indicates that the adsorption process involves both chemisorption and physical adsorption, with $AG^{U6\text{-}(OH)_2}$@PMSQ likely exhibiting electrostatic and hydrophobic interactions during PSM adsorption.[41,42] In the pseudo-second-order kinetic model, k_2 represents the rate constant, which increased from 1.351×10^{-7} to 3.375×10^{-7} min^{-1} for $AG^{U6\text{-}(OH)_2}$ after *in situ* growth of UiO-66-$(OH)_2$ onto AG. This enhancement may be due to the capillary effect of mesopores and the accessibility of macropores in $AG^{U6\text{-}(OH)_2}$, promoting faster PSM adsorption. The rate constant for $AG^{U6\text{-}(OH)_2}$@PMSQ was 3.961×10^{-7} min^{-1}, likely due to the additional hydrophobic interactions from the superhydrophobic mesoporous network of PMSQ.[43] Furthermore, the aerogel's adsorption performance was reflected not only in its rate but also in the number of PSM adsorbed. $AG^{U6\text{-}(OH)_2}$@PMSQ adsorbed significantly more PSM (555.556 mg g^{-1}) compared to AG (384.615 mg g^{-1}) and $AG^{U6\text{-}(OH)_2}$ (434.783 mg g^{-1}). Additionally, $AG^{U6\text{-}(OH)_2}$@PMSQ outperformed the other adsorbent materials (Table S7, ESI†).

To further evaluate the adsorption capacity and removal efficiency of $AG^{U6\text{-}(OH)_2}$@PMSQ for other common plastic pollutants, three widely used beverage-related plastics (PP, PET, and HDPE) were tested. Adsorption kinetics and first-order kinetic fitting revealed that the adsorption capacities of $AG^{U6\text{-}(OH)_2}$@PMSQ for PP, PET, and HDPE were 463.26, 501.10, and 432.89 mg g^{-1}, respectively (Fig. S15 and Table S8, ESI†). These results demonstrate that $AG^{U6\text{-}(OH)_2}$@PMSQ exhibits high adsorption capacity and efficiency across a range of plastic types, confirming its potential for broad-spectrum microplastic removal.

The Weber intra-particle diffusion model provides further insights into the adsorption kinetics of PSM by aerogels. As shown in Fig. 4g, the adsorption of PSM by AG and $AG^{U6\text{-}(OH)_2}$ can be divided into three linear stages. The first stage corresponds to the membrane diffusion mechanism, where PSM molecules move from the aqueous solution to the boundary layer of the adsorbent. In the second stage, PSM diffuses into the pores of the adsorbent, with intra-particle diffusion and chemical reactions controlling the adsorption rate. The third stage represents the equilibrium state.[9,44] Notably, the adsorption process of PSM by $AG^{U6\text{-}(OH)_2}$@PMSQ reached equilibrium immediately after the membrane diffusion stage. This behavior is attributed to the super-hydrophobicity of $AG^{U6\text{-}(OH)_2}$@PMSQ, which prevents PSM from entering the pores in the presence of water, leading to surface adsorption rather than internal pore adsorption. During the membrane diffusion stage, the adsorption rate of PSM by $AG^{U6\text{-}(OH)_2}$@PMSQ was 56.760 mg g^{-1} $min^{-1/2}$, significantly higher than the rates observed for AG (26.010 mg g^{-1} $min^{-1/2}$) and $AG^{U6\text{-}(OH)_2}$ (54.637 mg g^{-1} $min^{-1/2}$) (Table S9, ESI†). This suggests that while $AG^{U6\text{-}(OH)_2}$@PMSQ relies on surface adsorption, the additional hydrophobic forces substantially enhance the aerogel's rapid PSM adsorption.

The isothermal adsorption model effectively describes the interaction mechanism between aerogels and PSM. The three aerogels were mixed with PSM standard solutions at concentrations ranging from 1 to 20 mg mL^{-1}, allowing the system to reach adsorption equilibrium. As shown in Fig. 4h, adsorption by all three aerogels increased steadily between 1 and 15 mg mL^{-1}, then stabilized at 20 mg mL^{-1}. Among them, $AG^{U6\text{-}(OH)_2}$@PMSQ exhibited the highest PSM adsorption across all concentrations.

The experimental data were analyzed using the Langmuir (Fig. 4i) and Freundlich (Fig. 4j) isotherm models at a constant temperature. The Langmuir model, which assumes equal affinity of adsorption sites, describes a monolayer adsorption process on a homogeneous surface.[45] In contrast, the Freundlich model represents a multilayer adsorption process with an exponential distribution of active sites and energies on a heterogeneous surface.[46] As shown in Tables S10 and S11 (ESI†), the Langmuir model better fits the experimental data, with a higher average correlation coefficient compared to the Freundlich model ($R^2 = 0.8982$). This suggests that PSM adsorption occurs primarily through chemisorption on uniformly distributed active sites. Additionally, $1/n$ reflects the energy distribution and heterogeneity of the adsorption sites. The adsorption process is considered favorable when $0 < 1/n < 1$, irreversible when $1/n = 1$, and difficult when $1/n > 1$. The $1/n$ values for PSM adsorption by AG, $AG^{U6\text{-}(OH)_2}$, and $AG^{U6\text{-}(OH)_2}$@PMSQ were 0.214, 0.290, and 0.773, respectively, indicating that all three materials exhibit favorable structural properties for PSM adsorption.

The D–R model also assumes a heterogeneous surface and is particularly applicable at high to intermediate sorbate concentrations.[47] The values of K_{DR} (porosity factor) and Q_{MAX} (a measure of sorption capacity) were obtained by plotting $\ln q_e$ *versus* ε^2, as described in eqn (8) (Fig. S16, ESI†).[48] A higher Q_{MAX} value indicates a greater adsorption capacity of the adsorbent. As shown in Table S12 (ESI†), the adsorption capacities of the three adsorbents follow the order: $AG^{U6\text{-}(OH)_2}$@PMSQ > $AG^{U6\text{-}(OH)_2}$ > AG. This trend is consistent with the results from the pseudo-second-order kinetic model.

The K_{DR} values for all three adsorbents are less than 1 mol^2 kJ^{-2}, suggesting the presence of micropores on their surfaces. Applying the K_{DR} values to eqn (13) yields the apparent adsorption energy E (kJ mol^{-1}) for PSM.

$$E = \frac{1}{\sqrt{2K_{DR}}} \tag{13}$$

the values of $E > 8$ kJ mol^{-1} indicate that chemisorption is the dominant adsorption mechanism over physisorption. In this study, the E values for both AG and $AG^{U6\text{-}(OH)_2}$ exceeded 8 kJ mol^{-1}, confirming that PSM adsorption on these materials is primarily driven by chemisorption. Notably, the apparent energy for $AG^{U6\text{-}(OH)_2}$@PMSQ (26.73 kJ mol^{-1}) was significantly higher than that of AG (19.61 kJ mol^{-1}) and

$AG^{U6\text{-}(OH)_2}$ (18.90 kJ mol^{-1}). This may be attributed to the enhanced apparent free energy resulting from an entropy gain effect. Specifically, a large number of ordered water molecules are released as the adsorbate transfers from the aqueous phase to the hydrophobic surface.[49] Therefore, although the E value was higher than 8 kJ mol^{-1}, the adsorption process of $AG^{U6\text{-}(OH)_2}$@PMSQ on PSM was mainly dominated by physical interactions (hydrophobic interactions).

Simulation calculations

To investigate the potential adsorption mechanism of PSM on the $AG^{U6\text{-}(OH)_2}$@PMSQ surface, the weak interactions between PSM and PMSQ were analyzed by simulation calculations. The optimal adsorption configuration was determined using VASP software (Fig. 5a), with the system's adsorption energy calculated at −4.06 kcal mol^{-1} (Table S14, ESI†), indicating that the adsorption process is spontaneous.[50] The charge density difference (Fig. 5b) highlights the charge transfer within the adsorption system, where cyan regions represent electron depletion, and yellow regions indicate electron accumulation.[51] Notably, the electrons in the Si–O and C–H bonds of the hydrophobic groups in PMSQ are transferred similarly to those in PSM molecules, with all electrons in the PSM molecules being enriched on the PMSQ surface. This suggests a strong interaction between the $AG^{U6\text{-}(OH)_2}$@PMSQ surface and PSM during adsorption. Moreover, the electron localization function (ELF) distribution (Fig. 5c and d) provides a detailed visualization of electron density.[52] The hydrocarbon groups and benzene rings in PSM exhibit high electron density in the presence of PSMQ, indicating the potential formation of hydrogen bonds and C–H···π interactions between them.[53–55]

Anti-interference ability and regeneration of $AG^{U6\text{-}(OH)_2}$@PMSQ

Beverages contain a variety of coexisting ions, small molecules, and macromolecular compounds. Therefore, in practical applications, the removal efficiency of aerogels for PSM may be influenced by the surrounding environment. To assess this, the resistance of $AG^{U6\text{-}(OH)_2}$@PMSQ to interference in different environments was tested by adding several salts, sugars and proteins. As shown in Fig. S17a (ESI†), $AG^{U6\text{-}(OH)_2}$@PMSQ maintained a PSM removal efficiency of over 75% across six different interfering conditions, with even higher efficiency in high-salt environments. This may be due to the desalting effects of NaCl and KCl, which increased the hydrophobicity of PSM, making it more conducive to adsorption.[56] In contrast, in high-protein environments, the removal efficiency of $AG^{U6\text{-}(OH)_2}$@PMSQ slightly decreased, likely due to large molecular weight proteins clogging the aerogel's pore structure, thus inhibiting its adsorption capacity.[57] Regeneration and reuse experiments were conducted to evaluate the economic viability of $AG^{U6\text{-}(OH)_2}$@PMSQ. As shown in Fig. S17b (ESI†), after five adsorption cycles, $AG^{U6\text{-}(OH)_2}$@PMSQ retained a PSM removal efficiency of 77.60%. These results demonstrate that $AG^{U6\text{-}(OH)_2}$@PMSQ remains stable and effective in long-term adsorption applications. To evaluate the adsorption efficiency of $AG^{U6\text{-}(OH)_2}$@PMSQ on PSM under varying conditions,

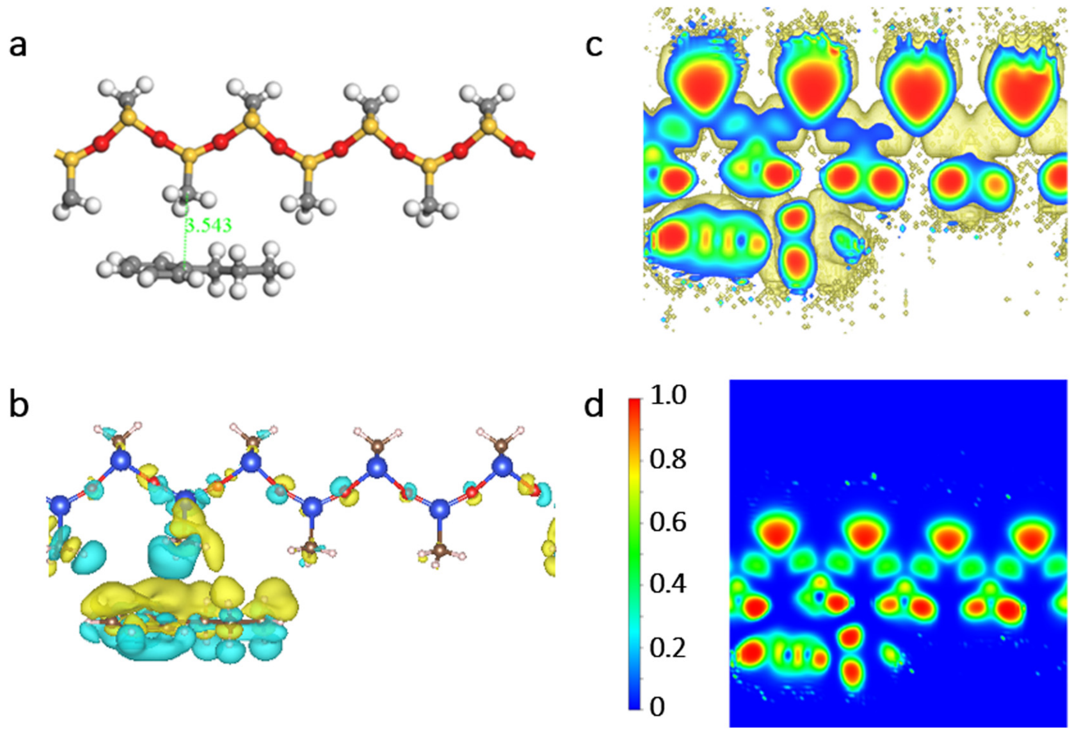

Fig. 5 (a) Adsorption configuration of PSM molecules on the PMSQ surface (Si, yellow; O, red; C, grey; H, white). (b) 3D charge density difference isosurface of the optimal adsorption model (Si, blue; O, red; C, brown; H, white). (c) 3D contour plot and (d) 2D slice of the electron localization function (ELF) for PSM on the PMSQ surface.

Table 1 Precision and recovery of PSM in beverages obtained using the $AG^{U6-(OH)_2}$@PMSQ extraction method

	Low[a] (%)		Medium[b] (%)		High[c] (%)	
Samples	Recovery	RSD	Recovery	RSD	Recovery	RSD
Bottled water	100.09 ± 1.70	4.47 ± 0.24	93.83 ± 4.89	2.27 ± 0.44	104.76 ± 3.87	3.07 ± 0.12
Gatorade	103.55 ± 3.47	2.93 ± 0.86	118.86 ± 5.17	2.82 ± 0.64	113.52 ± 0.46	4.20 ± 1.51
Soda drink	94.88 ± 0.67	4.12 ± 0.45	98.85 ± 2.48	4.70 ± 0.43	104.06 ± 2.11	7.88 ± 1.58
Sprite	117.51 ± 2.48	5.87 ± 1.76	103.18 ± 3.45	3.33 ± 0.96	92.16 ± 4.50	2.39 ± 0.14
Coffee	84.62 ± 2.45	6.92 ± 1.08	90.46 ± 0.12	2.95 ± 0.75	118.12 ± 4.57	2.77 ± 0.76
Tea	103.79 ± 1.66	8.27 ± 0.97	84.26 ± 0.79	5.35 ± 1.48	105.72 ± 2.37	4.96 ± 1.89

[a] 1.0 mg mL^{-1}. [b] 5.0 mg mL^{-1}. [c] 10.0 mg mL^{-1}.

adsorption experiments were conducted at different temperatures (20, 50, 75, and 100 °C) and ionic strengths (1, 3, 5, 7, and 10 mg mL^{-1}). As shown in Fig. S18a (ESI†), temperature had little effect on the adsorption performance, likely due to the enhanced thermal stability conferred by the layer-by-layer assembly technique, as also supported by the DTG results. Additionally, the adsorption capacity slightly increased at higher salt concentrations (Fig. S18b, ESI†). This behavior may be attributed to the reduction of the exposed nonpolar or hydrophobic surface area in the aqueous phase. In such environments, hydrophobic interactions are entropically favored, promoting the aggregation of the hydrophobic adsorbent and adsorbate to minimize the contact area with water molecules.[56]

Removal of PSM from real samples

Safety is a critical requirement for materials used in food purification. To evaluate the *in vitro* cytotoxicity and ensure the safety of the prepared aerogels for food contact applications, CCK-8 cell viability assays were conducted using GES-1 and intestinal mucosal epithelial cells. As shown in Fig. S19 (ESI†), after 48 hours of incubation with extracts from AG, $AG^{U6-(OH)_2}$ and $AG^{U6-(OH)_2}$@PMSQ, the viability of GES-1 cells was 95.65%, 96.94%, and 95.61%, respectively. The corresponding viability values for intestinal epithelial cells were 98.66%, 97.98%, and 98.57%. Since cell viability above 80% is generally considered indicative of non-toxicity, these results confirm that AG, $AG^{U6-(OH)_2}$ and $AG^{U6-(OH)_2}$@PMSQ are biocompatible and safe for use in removing PSM from food matrices.

The effect of the matrix on the results was evaluated by comparing the response of PSM in deionized water to its response in various beverages. To eliminate the matrix interference, calibration curves for PSM in each beverage were established using the external standard method.[58] As shown in Table S13 (ESI†), the regression coefficients (R^2) for PSM range from 0.9976 to 0.9999, with the slopes of the standard curves in beverages closely matching those in deionized water. The limit of detection (LOD) and limit of quantification (LOQ) were determined based on signal-to-noise ratios (S/N) of 3 and 10, respectively.

The accuracy and precision of the $AG^{U6-(OH)_2}$@PMSQ method for use in different beverages were assessed using a spiked recovery method. PSM solutions at three different concentration levels were spiked into various beverages, and recoveries measured using the $AG^{U6-(OH)_2}$@PMSQ extraction method ranged from 84.26% to 118.86%, with RSD values between 2.27% and 8.27% (Table 1). These results fall within the European Commission's recommended recovery range of 70–120% and RSD limit of 20%, indicating that the $AG^{U6-(OH)_2}$@PMSQ extraction method is both stable and reproducible in beverage matrices.[59]

Conclusions

In conclusion, composite aerogels with superhydrophobicity were fabricated for the rapid and high-capacity adsorption of PSM in beverages. This was achieved by incorporating UiO-66-$(OH)_2$ and PMSQ mesoporous networks into cellulosic aerogels with a dual-network structure using a layer-by-layer assembly technique. $AG^{U6-(OH)_2}$@PMSQ demonstrated exceptional organic solvent adsorption performance, attributed to its hierarchical porosity and superhydrophobicity (contact angle of 157.1°). The adsorption kinetics revealed that $AG^{U6-(OH)_2}$@PMSQ achieved an impressive adsorption capacity of 555.556 mg g^{-1} for PSM within a relatively short time frame of 100 min. According to the D–R model analysis, the adsorption of PSM by $AG^{U6-(OH)_2}$@PMSQ was primarily governed by hydrophobic interactions. Meanwhile, the adsorption mechanism of PSM on the $AG^{U6-(OH)_2}$@PMSQ surface was further investigated through simulation calculations, revealing an adsorption energy of -4.1 kcal mol^{-1}, indicating spontaneous adsorption. The charge density difference suggests the presence of hydrogen bonding and $C–H\cdots\pi$ interactions. Additionally, $AG^{U6-(OH)_2}$@PMSQ demonstrated excellent stability, reproducibility, and resistance to interference in various beverages, with recoveries ranging from 84.26% to 118.86%. This work highlights the potential of high-performance superhydrophobic composite aerogels assembled *in situ via* a layer-by-layer assembly technique, offering a novel strategy for efficient removal of hazardous substances from food.

Author contributions

The manuscript was written through the contributions of all authors. All authors have given approval to the final version of the manuscript. Qiyue Zhao: investigation, methodology, writing – original draft preparation and project administration; Xingxu Jiang: supervision; Ergen Bao: methodology; Hong-Man Hou: methodology and data curation; Gong-Liang Zhang:

investigation and data curation; Jingran Bi: conceptualization, supervision, writing – review & editing, funding acquisition and validation.

Conflicts of interest

There are no conflicts to declare.

Data availability

The authors confirm that the data supporting the findings of this study are available within the article and its ESI.†

Acknowledgements

This article was supported by the National Natural Science Foundation of China (32102050), the National Science Foundation of Liaoning province (2024-MS-170), and the Open Foundation of State Key Laboratory of Marine Food Processing & Safety Control (SKL202406).

References

1 Z. Wang, C. Sun, F. Li and L. Chen, *Chem. Eng. J.*, 2021, **415**, 129006.

2 M. MacLeod, H. P. H. Arp, M. B. Tekman and A. Jahnke, *Science*, 2021, **373**, 61–65.

3 I. Leppänen, T. Lappalainen, T. Lohtander, C. Jonkergouw, S. Arola and T. Tammelin, *Nat. Commun.*, 2022, **13**, 1814.

4 C. Della Torre, E. Bergami, A. Salvati, C. Faleri, P. Cirino, K. A. Dawson and I. Corsi, *Environ. Sci. Technol.*, 2014, **48**, 12302–12311.

5 R. Mercogliano, C. G. Avio, F. Regoli, A. Anastasio, G. Colavita and S. Santonicola, *J. Agric. Food Chem.*, 2020, **68**, 5296–5301.

6 S. Sharma, S. Basu, N. P. Shetti, M. N. Nadagouda and T. M. Aminabhavi, *Chem. Eng. J.*, 2021, **408**, 127317.

7 J. Kang, L. Zhou, X. Duan, H. Sun, Z. Ao and S. Wang, *Matter*, 2019, **1**, 745–758.

8 V. Tournier, C. M. Topham, A. Gilles, B. David, C. Folgoas, E. Moya-Leclair, E. Kamionka, M. L. Desrousseaux, H. Texier, S. Gavalda, M. Cot, E. Guémard, M. Dalibey, J. Nomme, G. Cioci, S. Barbe, M. Chateau, I. André, S. Duquesne and A. Marty, *Nature*, 2020, **580**, 216–219.

9 C. Sun, Z. Wang, L. Chen and F. Li, *Chem. Eng. J.*, 2020, **393**, 124796.

10 Y.-J. Chen, Y. Chen, C. Miao, Y.-R. Wang, G.-K. Gao, R.-X. Yang, H.-J. Zhu, J.-H. Wang, S.-L. Li and Y.-Q. Lan, *J. Mater. Chem. A*, 2020, **8**, 14644–14652.

11 S. Ahankari, P. Paliwal, A. Subhedar and H. Kargarzadeh, *ACS Nano*, 2021, **15**, 3849–3874.

12 M. Chen, T. Liu, X. Zhang, R. Zhang, S. Tang, Y. Yuan, Z. Xie, Y. Liu, H. Wang, K. V. Fedorovich and N. Wang, *Adv. Funct. Mater.*, 2021, **31**, 2100106.

13 E. M. Dias and C. Petit, *J. Mater. Chem. A*, 2015, **3**, 22484–22506.

14 P. Wu, M. Guo, R.-W. Zhang, Q. Huang, G. Wang and Y. Lan, *Chem. Sci.*, 2024, **15**, 17781–17798.

15 A. A. Mohana, M. Rahman, S. K. Sarker, N. Haque, L. Gao and B. K. Pramanik, *Chemosphere*, 2022, **309**, 136682.

16 H. Li, Y. Duan, Y. Shao, Z. Zhang and L. Ren, *J. Mater. Chem. A*, 2024, **12**, 14885–14939.

17 L. Li, M. E. Griebel, M. Uroz, S. Y. Bubli, K. A. Gagnon, B. Trappmann, B. M. Baker, J. Eyckmans and C. S. Chen, *Adv. Funct. Mater.*, 2024, **34**, 2309567.

18 A. Mulyadi, Z. Zhang and Y. Deng, *ACS Appl. Mater.*, 2016, **8**, 2732–2740.

19 M. Hamedi, E. Karabulut, A. Marais, A. Herland, G. Nyström and L. Wågberg, *Angew. Chem., Int. Ed.*, 2013, **52**, 12038–12042.

20 Z. Zhang, G. Sèbe, D. Rentsch, T. Zimmermann and P. Tingaut, *Chem. Mater.*, 2014, **26**, 2659–2668.

21 Q. Zhao, X. Chen, G.-L. Zhang, H. Hao, B.-W. Zhu, H.-M. Hou and J. Bi, *ACS Appl. Mater.*, 2022, **14**, 29131–29143.

22 Q. Zhao, H.-M. Hou, Y. Qiu, G.-L. Zhang, H. Hao, B.-W. Zhu and J. Bi, *J. Hazard. Mater.*, 2024, **465**, 133160.

23 J. Rostami, K. Gordeyeva, T. Benselfelt, E. Lahchaichi, S. A. Hall, A. V. Riazanova, P. A. Larsson, G. Cinar Ciftci and L. Wågberg, *Mater. Today*, 2021, **48**, 47–58.

24 D. Chen, W. Yang, L. Jiao, L. Li, S.-H. Yu and H.-L. Jiang, *Adv. Mater.*, 2020, **32**, 2000041.

25 J. Zhang, J. Zheng, M. Gao, C. Xu, Y. Cheng and M. Zhu, *Adv. Mater.*, 2023, **35**, 2300813.

26 J. Zhang, Y. Cheng, C. Xu, M. Gao, M. Zhu and L. Jiang, *Adv. Funct. Mater.*, 2021, **31**, 2009349.

27 G. Kresse and J. Hafner, *Phys. Rev. B: Condens. Matter Mater. Phys.*, 1993, **48**, 13115–13118.

28 G. Kresse and J. Furthmüller, *Phys. Rev. B: Condens. Matter Mater. Phys.*, 1996, **54**, 11169–11186.

29 G. Kresse and J. Furthmüller, *Comput. Mater. Sci.*, 1996, **6**, 15–50.

30 J. P. Perdew, K. Burke and M. Ernzerhof, *Phys. Rev. Lett.*, 1996, **77**, 3865–3868.

31 P. E. Blöchl, *Phys. Rev. B: Condens. Matter Mater. Phys.*, 1994, **50**, 17953–17979.

32 G. Kresse and D. Joubert, *Phys. Rev. B: Condens. Matter Mater. Phys.*, 1999, **59**, 1758–1775.

33 M. Methfessel and A. T. Paxton, *Phys. Rev. B: Condens. Matter Mater. Phys.*, 1989, **40**, 3616–3621.

34 T. Benselfelt, J. Engström and L. Wågberg, *Green Chem.*, 2018, **20**, 2558–2570.

35 X. Ma, Y. Lou, X.-B. Chen, Z. Shi and Y. Xu, *Chem. Eng. J.*, 2019, **356**, 227–235.

36 B. Chen, H. Zhang, L. Li and Y. Hu, *ACS Appl. Polym. Mater.*, 2023, **5**, 3554–3563.

37 Y. Cao, X. Chen, X. Li and B. Wang, *ACS Appl. Nano Mater.*, 2021, **4**, 5486–5495.

38 C. Chen, D. Chen, S. Xie, H. Quan, X. Luo and L. Guo, *ACS Appl. Mater.*, 2017, **9**, 41043–41054.

39 L. Zhu, L. Zong, X. Wu, M. Li, H. Wang, J. You and C. Li, *ACS Nano*, 2018, **12**, 4462–4468.

40 J. Ye, P. Cai, Z. Huang and Y. Pan, *ACS Appl. Polym. Mater.*, 2023, **5**, 3632–3642.

41 H.-P. Wang, X.-H. Huang, J.-N. Chen, M. Dong, C.-Z. Nie and L. Qin, *Chem. Eng. J.*, 2023, **476**, 146562.

42 J. Fu, N. Liu, Y. Peng, G. Wang, X. Wang, Q. Wang, M. Lv and L. Chen, *J. Hazard. Mater.*, 2023, **456**, 131685.

43 X. Zhang, Y. Lei, C. Li, G. Sun and B. You, *Adv. Funct. Mater.*, 2022, **32**, 2110830.

44 H. Zhao, X. Huang, L. Wang, X. Zhao, F. Yan, Y. Yang, G. Li, P. Gao and P. Ji, *Chem. Eng. J.*, 2022, **430**, 133122.

45 M. A. Al-Ghouti and D. A. Da'ana, *J. Hazard. Mater.*, 2020, **393**, 122383.

46 S. S. A. Alkurdi, R. A. Al-Juboori, J. Bundschuh, L. Bowtell and A. Marchuk, *J. Hazard. Mater.*, 2021, **405**, 124112.

47 K. Y. Foo and B. H. Hameed, *Chem. Eng. J.*, 2010, **156**, 2–10.

48 R. R. Sheha and E. A. El-Shazly, *Chem. Eng. J.*, 2010, **160**, 63–71.

49 Z.-Z. Bao, Z.-F. Chen, Y. Zhong, G. Wang, Z. Qi and Z. Cai, *Sci. Total Environ.*, 2021, **764**, 142889.

50 S. Zhu, M. A. Khan, T. Kameda, H. Xu, F. Wang, M. Xia and T. Yoshioka, *J. Hazard. Mater.*, 2022, **426**, 128062.

51 X. Li, Z. Shen, H. Zhang, X. Li, Y. Zhou and H. Yao, *Chem. Eng. J.*, 2022, **440**, 135665.

52 S. Wang, T. Liu, E. Zhu, C. He, Q. Shi and X. Feng, *Water Res.*, 2024, **254**, 121412.

53 L. Brugnoli, S. Urata and A. Pedone, *J. Phys.: Condens. Matter*, 2022, **34**, 164006.

54 J. C. Santos, J. Andres, A. Aizman and P. Fuentealba, *J. Chem. Theory Comput.*, 2005, **1**, 83–86.

55 S. Emamian, T. Lu, H. Kruse and H. Emamian, *J. Comput. Chem.*, 2019, **40**, 2868–2881.

56 Y. Zhang, C. Zhu, F. Liu, Y. Yuan, H. Wu and A. Li, *Sci. Total Environ.*, 2019, **646**, 265–279.

57 Q. Lan, A. S. Bassi, J.-X. Zhu and A. Margaritis, *Chem. Eng. J.*, 2001, **81**, 179–186.

58 W. Zhang, C. Lan, H. Zhang, Y. Zhang, W. Zhang, W. Zhao, C. Johnson, K. Hu, F. Xie and S. Zhang, *J. Agric. Food Chem.*, 2019, **67**, 3733–3743.

59 Q. Zhao, H.-M. Hou, G.-L. Zhang, H. Hao, B.-W. Zhu and J. Bi, *Int. J. Biol. Macromol.*, 2024, **267**, 131584.